A CFD study on horizontal oil-water flow with high viscosity ratio

Jing Shi[1,2], Mustapha Gourma[1], Hoi Yeung[1]

1. Oil and Gas Engineering Centre, School of Water, Environment and Energy, Cranfield University, Cranfield MK43 0AL, UK

2. Department of chemistry, Durham University, Durham, DH1 3LE, UK

Abstract

A CFD study on horizontal oil-water flow with high viscosity ratio ($O(10^3)$) was conducted with the VOF multiphase model in conjunction with the SST k–ω turbulence scheme. Suitable settings of the CFD models and numerical solution were highlighted. Particularly, the wall contact angle is shown to be important regarding the oil fouling phenomenon commonly seen in water-lubricated transportation of highly viscous oil. Satisfactory predictions of flow patterns were obtained. Water holdup calculations were consistent with measurements, attaining relative discrepancy within 14%. However, pressure gradients exhibited inconsistencies with relative discrepancy within 70%, for which poor prediction of oil fouling for some simulations is the main cause. Nevertheless, the CFD models provided reasonable estimate of the water lubrication degree for water-lubricated flow. Detailed flow characteristics of core annular flow (CAF) with high viscosity ratio were discussed in particular based on the 3D simulation results.

Keywords: Oil-water; high viscosity ratio; core annular flow (CAF); oil fouling.

Correspondence concerning this article should be addressed to J. Shi at jingshi1988@gmail.com

1 Introduction

Flows of immiscible liquids with high-viscosity ratios are encountered in many industries such as food processing, pharmaceutical, and petroleum industries. In heavy crude oil production, water-lubricated transportation, i.e., transportation of heavy oil together with surrounding water that lubricates the pipe, has attracted attentions for its economic benefit of minimal pumping power. The most advantageous flow regime of water-lubricated transportation is core annular flow (CAF) — continuous oil-core surrounded by continuous water-annulus. Less desirable phase configurations with continuous water include oil plugs in water (OPL) and dispersed oil lumps in water (OLP).

A large number of experimental studies on water-lubricated flow reported results on flow patterns and/or pressure gradients, see Joseph et al. (1999), McKibben et al. (2000a and 2000b), Grassi et al. (2008), Sotgia et al. (2008), Wang et al. (2011), and Cavicchio et al. (2018), to cite but a few. Other investigations included phase holdup measurements in addition to flow patterns and/or pressure gradients, see for example, Arney et al. (1993), Oliemans et al. (1987), Bannwart (1998), Sridhar et al. (2011), Strazza et al. (2011) and Shi et al. (2017c). It is challenging and often expensive to measure detailed flow characteristics that are of importance to improvement of engineering design and operation. Three-dimensional numerical modelling has assumed an increasing role in the context of multiphase flows, offering access to both local flow fields and global parameters.

Thus far, numerical studies of high-viscosity oil-water CAF focus on descriptions of interfacial waves and their transitions. Dedicated in-house CFD codes have been used for analyse of interfacial waves in CAF. Ooms et al. (1984) adopted the lubrication theory framework to model horizontal CAF with prescribed interfacial waves under the assumption of the oil core being solid. A similar approach was used later by Bai et al. (1996) for the study of low Reynolds number concentric CAF with axisymmetric interfacial waves. Ko et al. (2002) extended the aforementioned model by adopting the turbulence SST k–ω scheme. Li and Renardy (2000) applied a volume-of-fluid (VOF) scheme to enhance the wave shape simulation. In a similar vein, Ooms et al. (2013) and Housz et al.(2017) adopted the VOF model to simulate horizontal CAF at low and high Reynolds number respectively. The level set method for studying CAF at low Reynolds number was a preferred framework in Lee and Kang

(2016). The importance of interfacial waves in the levitation of the core liquid is highlighted from the above numerical investigations.

In addition to dedicated in-house CFD codes, commercial CFD packages have been employed increasingly for both research and engineering design. A reasonable number of studies with commercial CFD packages on CAF in vertical flow lines and CAF through particular geometries/devices have been reported. Amongst which, we mention the works of Ghosh et al. (2010, 2011) on downward CAF in a vertical pipe and CAF in a vertical U bend. The VOF model was adopted by the above authors. Satisfactory agreement was reached between predictions and experimental results. Jiang et al. (2014) used the Eulerian-Eulerian approach to simulate CAF in a vertical U bend and did not find any major deviation to predictions obtained with the VOF model in Ghosh et al. (2011). CAF in a flow line with a sudden contraction followed with expansion was investigated by Kaushik et al. (2012). The authors found that downstream phase distributions are significantly altered by the cross-sectional changes. Dehkordi et al. (2017) simulated CAF through a horizontal venturi and a nozzle flow meter with the VOF approach. Fair predictions of pressure drop and water holdup were obtained. Non-Newtonian oil-water core annular flow through return bends was simulated by Jiang et al. (2018) in which the influences of non-Newtonian oil properties on the pressure gradient and oil fouling were studied.

In all the aforementioned CFD studies, the oil-to-water viscosity ratios range between 200 and 900 (i.e., $O(10^2)$). In engineering applications of water-lubricated heavy oil transportation, the oil-to-water viscosity ratio can be much higher with $O(10^3)$ or above, for which studies with CFD packages are quite limited. Also, investigations with CFD packages on CAF and other flow regimes of water-lubricated flow in elongated horizontal flow lines, that is, fully developed horizontal flows, are rather scarce. The CFD models and numerical solution settings that are tested with low- or medium-viscosity fluids do not necessarily provide satisfactory predictions for high-viscosity fluids. In this study, we report simulations of oil-water flow with viscosity ratio of $O(10^3)$ in horizontal pipelines with L/d =154 and 197, and the flow at the downstream of the pipelines is either fully developed or nearly fully developed. The objectives of the simulations are to examine the capability of the CFD models to simulate highly viscous oil-water two-phase flow and identify areas with respect to the numerics and physical correlations where

further improvement is needed. By carefully selecting a set of initial parameters and schemes, the capabilities of VOF model to predict reasonable flow patterns are shown. Highlighted is the influence of static contact angles on the capture of oil fouling film on pipe wall and the prediction of pressure gradients. The flow characteristics of CAF with high viscosity ratio were discussed in particular based on the 3D simulation results.

2 CFD model and simulation setup

2.1 CFD models

The VOF model implemented in FLUENT was used to conduct the numerical simulations. This model has been shown to provide satisfactory calculations for oil-water flow with medium viscosity ratio in our separate study (Shi et al., 2017b). The oil-water system is described through a set of conservation equations for the mixture (Eqs. 1 and 2) and oil phase (Eq. 3).

Mass equation: $\dfrac{\partial(\rho)}{\partial t} + \nabla \cdot (\rho \mathbf{u}) = 0$ (1)

Momentum equation: $\dfrac{\partial}{\partial t}(\rho \mathbf{u}) + \nabla \cdot (\rho \mathbf{u} \cdot \mathbf{u}) = -\nabla p + \nabla \cdot \left[\mu\left(\nabla \mathbf{u} + \nabla \mathbf{u}^T\right)\right] + \rho \mathbf{g} + \mathbf{F}$ (2)

Volume fraction equation: $\dfrac{\partial(\rho_o \alpha_o)}{\partial t} + \nabla \cdot (\rho_o \alpha_o \mathbf{u}) = 0$ (3)

The oil-water interface tracking is accomplished by solving for the volume fraction of the oil phase (set as the secondary phase) in Eq. (3). The material properties of the mixture, i.e., density ρ and viscosity μ in the transport equations, are weighted by the volume fraction of each phase present in the control volume, see Eqs. (4) and (5). The volume fraction of the water phase (set as the primary phase) is determined by the constraint of fluid continuity (Eq. 6) after solving for oil phase in equation (3).

$\rho = \alpha_o \rho_o + \alpha_w \rho_w$ (4)

$\mu = \alpha_o \mu_o + \alpha_w \mu_w$ (5)

$\alpha_w + \alpha_o = 1$ (6)

The body force term, $\mathbf{F}$, in the momentum equation (Eq. (2)) results from the presence of the interface. It denotes the contribution of the interfacial tension and requires further modelling. The continuum surface force (CSF) model proposed by Brackbill et al. (1992) was used (see Eqs. (7–10)).

$$\mathbf{F} = \sigma \kappa \frac{\rho \nabla \alpha_0}{\frac{1}{2}(\rho_w + \rho_o)} \tag{7}$$

where

$$\kappa = \nabla \cdot \hat{\mathbf{n}} \tag{8}$$

$$\hat{\mathbf{n}} = \frac{\nabla \alpha_o}{\| \nabla \alpha_o \|}. \tag{9}$$

For the cells in contact with rigid boundaries, the wall adhesion at fluids interfaces is accounted for by the following equation:

$$\hat{\mathbf{n}} = \hat{\mathbf{n}}_{wl} \cos \theta_{wl} + \hat{\mathbf{t}}_{wl} \sin \theta_{wl} \tag{10}$$

where $\hat{\mathbf{n}}_{wl}$ and $\hat{\mathbf{t}}_{wl}$ are the unit vectors normal and tangential to the wall, respectively. The contact angle, θ_{wl}, is the angle tangent to the fluids interface with respect to the wall. The contact angle is time dependent and has its own dynamics. In this study, an initial static contact angle was prescribed.

In conjunction with the VOF multiphase flow model, the shear stress transport (SST) k–ω model was used for turbulence modelling. A brief description of the SST k–ω model is given in Appendix.

2.2 Simulation geometries and boundary conditions

The numerical simulations presented in this study were benchmarked by our previous experimental campaign detailed in Shi et al. (2017a and 2017c). Oil and water phases were pumped separately into a T-junction of a horizontal pipe. Nominal oil and water viscosities are μ_o=5000 cP and μ_w=1cP, with densities of ρ_o=910 kg/m^3 and ρ_w=998 kg/m^3 and oil-water interfacial tension σ=0.02 N/m.

The schematic representation of the simulation geometry is shown in Figure 1. The primary geometry, denoted as Geometry I, has an internal diameter d=0.026 m and length L=4 m. Simulation results of flow through Geometry I were used to validate the CFD models. A scale-up of Geometry I to Geometry II with internal diameter d=76 mm and length L=15 m was used to investigate the flow in a larger diameter pipe. Each branch of the T-junction has a length of h=0.2 m for both geometries.

Hexahedral meshes with progressive refinement near the pipe wall with the height of first cell falling within the desired range of y+<5 were generated for the two geometries. A sensitivity analysis was conducted for grid size integrity from the solutions. The meshes consist of about 1.2 million and 1.9 million cells with heights of adjacent cells to the pipe wall of 0.2 mm and 1 mm for Geometry I and Geometry II, respectively.

The velocity boundary was set up at the inlets. Velocity profiles of developed laminar flow for the oil phase (Reynolds number $0.2 < Re_o < 100$) and developed laminar or turbulent flow for the water phase (Reynolds number $500 < Re_w < 40\ 000$) were loaded into the solver via UDF (user-defined functions) to have fully developed flows before the junction. The hydraulic diameter and corresponding turbulence intensity were also specified following Fluent user guide (2012), that is $I_o = 0$ and $I_w = 0.16Re_w{}^{-1/8}$. A gauge pressure of zero was applied at the outlet. No-slip boundary condition was imposed at the wall. A constant contact angle was imposed at wall adhesion condition, a value of θ_{wl} =175° was adopted unless otherwise specified; different wall contact angles were tested and discussed in the section 3.1.

2.3 Solution setup and simulation programme

Transient isothermal flows were solved with pressure-based segregated algorithm and explicit VOF scheme. The Geo-Reconstruct scheme was used for interface reconstruction. The SIMPLE scheme was used for the pressure-velocity coupling and the PRESTO! scheme was adopted for the pressure interpolation. The upwind scheme of 1st order then 2nd order for momentum equations was followed for a smoother convergence rate. A time step of dt=10^{-4} s was used. Convergence criteria were put at absolute errors of $\varepsilon_{err} \leq 10^{-4}$ for continuity and momentum equations, and at $\varepsilon_{err} \leq 10^{-6}$ for turbulence equations. Static pressures and water volume fractions were monitored at specific positions. Simulations were processed for amply long periods, ensuring fully established flows. Simulations with geometry I were benchmarked with flow conditions of experiments, profiled conditions were instead used when experimental data is not available for the purpose of mechanistic analysis. The programme of simulations performed in this study is listed in the Table 1.

3 Sensitivity to numerical setting

3.1 Wall contact angles

Presetting a static contact angle at the boundary does not mean that liquids are static at the contact line. The assumed contact angle is used to adjust the surface normal in cells near the wall. The liquids and the contact angle will move each time step towards their equilibrium positions under local stresses. For convenience, a series of simulations were performed with prescribed static contact angles. The goal here is to investigate the sensitivity of the numerical results to the prescribed contact angles for highly viscous oil-water flow (capillary number $Ca = \frac{\mu U}{\sigma} \gg 1$) and further estimate the most accurate static contact angles for simulations in the present study. Predicted flow patterns from cases with different contact angles are shown in Figure 2. The corresponding experimental flow pattern is also displayed for comparison. All simulations predicted water-lubricated flow, which is consistent with the experimental observations that water-lubricated flow is the dominant flow category in high-viscosity oil-water flow in either hydrophobic or hydrophilic pipelines (McKibben et al., 2000a, 2000b; Sridhar et al., 2011; Shi and Yeung, 2017). The dissimilarity between the predicted phase configurations lies in the degree of oil fouling on the pipe wall. A reduction in the prescribed static contact angle of the oil phase at the wall is accompanied with enhanced surface wetting by the oil phase, hence an increase in oil fouling on the pipe wall. As shown in Figure 2, the flow pattern obtained with an initial static contact angle of 175° is the closest match to the experimental flow pattern for the case under consideration. A wall contact angle of 175° was adopted in the following simulations in this study and fair agreement between simulation results and experimental data was reached for most of the numerical tests. It is worth remarking that the ad-hoc method of imposing a static contact angle is a deficient representation of the reality, therefore the results on oil fouling capture should be interpreted with caution. A better approach is via models of dynamic contact angle. Existing models of dynamic contact angle are empirically based and limited to flows with low Reynolds and capillary numbers (Jiang et al., 1979, Van Mourik et al.,2005). We leave the study on modelling of dynamic contact angel for high capillary number fluids for future work.

3.2 Initialization methods

Much of this section is devoted to analyse the evolution of the mixture flow under a selected initialization procedure of the device. Simulations referred to by S-6a and S-6b in Table 1 were carried out using respective prescribed initial conditions of the water phase and initial conditions of the oil phase. The visualization of the results showing the phases' redistributions at specific instants is shown in Figure 3. Contrasting behaviours of mixture flows at earlier stages of simulations are demonstrated. At t=4 s for the case initialised with the water phase conditions, a long transient finger (instability) of turbulent water is displacing a certain amount of more viscous oil. By contrast, at t=5 s for the case initialised with the oil phase conditions, droplets of viscous oil are present in a turbulent water phase. Intriguingly, both the simulations converge to the flow pattern of oil lumps in water (OLP), which is consistent with experimental observations. Celerities and trajectories to the settling regime are sensitive to the initial conditions. To be precise, we examined the average pressure gradient and water holdup most downstream of the junction. The mean pressure gradients (0.86 kPa/m and 0.82 kPa/m for simulation S-6a and S-6b, respectively) and water holdups (0.86 and 0.87 for simulation S-6a and S-6b, respectively) from the simulations with different initialization methods are comparable when statistically steady solutions are reached.

The initial conditions are essential aspects of a simulation and crucial in affecting the routes to solution. It is of importance to check whether statistically-steady solutions are reached by monitoring relevant parameters. Obviously, the initialization with water phase conditions in our case offers a shorter path to convergence to the developed flow regime, hence this choice was adopted all along the present study.

3.3 Volume fraction interpolation

The evaluation of the ability of interpolation schemes to accurately rebuild oil-water interfaces is conducted by comparison against experiments. Simulations referenced to as S-2a and S-2b in Table 1 were respectively performed using Geo-Reconstruct scheme and CICSAM (Compressive Interface Capturing Scheme for Arbitrary Meshes) scheme. Both schemes are usually recommended for reconstruction of sharp contours. The CICSAM scheme is recommended for flows involving phases of

high viscosities in Fluent theory guide (2012). Flow patterns obtained with Geo-Reconstruct scheme and CICSAM scheme are both CAF, which is in conformity with experimental output, as illustrated in Figure 4. However, the predicted oil-water interface with the Geo-Reconstruct scheme better matches the experimental observation. The Geo-Reconstruct scheme revealed a core oil with a relatively smooth top-side and a wavy bottom-side, analogous to the configuration observed in the experiment. The CICSAM scheme however showed a smooth oil-core with little sign of wavy features on the bottom-side. It goes without saying that the Geo-Reconstruct scheme is adopted in the present study.

4 Results and discussion

4.1 Flow patterns and visual validations

Flow patterns obtained with CFD simulations and their corresponding experimental counterparts are illustrated in Figure 5. Overall, the calculations on a variety of flow patterns agree with experimental observations. These predictions range from core flow in S-3 and S-8a, to oil plugs in water in S-1 and oil lumps in water in S-5 and S-6a. Dispersed water in oil is predicted in S-7, which is an anticipated flow regime for flows with very high ratios of oil-to-water flow rates. Note here the experimental counterpart to simulation S-7 was not available due to limitation of the experimental facility on achievable minimum water flow rate.

Oil fouling film on pipe wall is a distinctive phenomenon in high-viscosity oil-water flow. It manifests itself by ripples on the pipe wall as illustrated with experimental snapshots in Figure 5. In our experimental campaign, oil fouling was observed in various regimes of water-lubricated flow, including core flow, oil plugs in water, and oil lumps in water. Cross sectional cuts of predicted pipeline flow are displayed in Figure 6. Of particular interest are the predictions from S-8a and S-15 which represent CAF in Geometry I and Geometry II respectively. Partial oil fouling (spots of oil on the wall) is predicted with CFD for the test S-8a while more pronounced oil fouling film is predicted for the test S-15. As said before, the wall adhesion effect is affected by the specified static wall contact angle. A prescribed static contact angle of 175° was used in both tests, thus the difference in the degree of oil fouling between the two tests is less likely caused by the specified wall contact angle. Whether oil fouling is heavier in flow conditions of test S-15 is not clear and needs validation of future experimental

work. In addition, it is noted that the mesh resolution of the region adjacent to the pipe wall can also affect the prediction of oil fouling thus the quantitative results on the oil fouling should be treated with caution. Nevertheless, the qualitative results on the captured oil fouling spots/film on the pipe wall by CFD are very encouraging.

4.2 Parametric investigation on flow patterns

4.2.1 Ratio of gravitation to viscous force

Having shown that the CFD models are capable to predict reasonable flow patterns, we conducted a parametric investigation on flow patterns. A wide range of flow conditions can be tested with the validated CFD models.

In a review on experimental liquid-liquid flows, Shi and Yeung (2017) found that the ratio of gravitation to viscous force, $G/V = \frac{\Delta \rho g D^2}{\mu U}$, is a good candidate to characterise flow patterns of liquid-liquid flows over a wide range of flow conditions. The gravitation to viscous force ratio reflects the competitive role of gravitational force and viscous force on phase configuration of oil-water flows. The viscous force is expressed as the product of the characteristic viscosity, μ_o, and velocity, U_m. The impact of gravitational–viscous force balance on the oil-water flows is demonstrated in Figure 7. Figure 7(a) shows change of flow pattern with oil viscosity hence G/V. A reduction in oil viscosity from 5000 cP to 100 cP, hence an increase in G/V from 0.2 to 9.7 induces a lifting of the oil core, leading to a progressive change of flow regime from CAF to stratified flow.

Figure 7(b) displays the change of phase configuration with G/V due to change of pipe diameter. For the flow condition of U_{so}=0.4 m/s, and U_{sw}=0.2 m/s, CAF develops in Geometry I, while wavy stratified flow develops in Geometry II. The gravitation to viscous force ratio is 1.7 for the latter case, indicating a flow system of viscous force and gravitational force comparable in which stratified flow is one of the possible phase configurations. There are entrained discontinuous water streams inside and at the top of the oil phase in Figure 7(b-ii). This flow regime is a transitional flow pattern from stratified flow to CAF; CAF develops when the discontinuous water streams become continuous.

Another simulation was performed in Geometry II at U_{so}=2.0 m/s, and U_{sw}=0.5 m/s under which G/V=0.4. It is anticipated that CAF or intermittent flow would develop as the viscous force becomes

dominant in the flow system. The calculated phase configuration is CAF as shown in Figure 7(b-iii). Compared to the test shown in Figure 7(b-ii), we can see that for oil-water flow in a larger diameter pipe, higher oil flow rate is required to form stable CAF.

4.2.2 Froude number

The definition of Froude number for internal multiphase flows is far from unequivocal in the literature. Here, $\text{Fr} = \sqrt{\dfrac{U_{so}{}^2}{gD\frac{\Delta\rho}{\rho_w}}}$ is adopted for investigation. It is related to the ratio of kinetic energy to potential energy of the oil phase. At high kinetic energy, i.e., Fr $\gg$1, the oil phase is shooting at speed through the pipe in a concentric fashion with little effect of the potential energy. The change of phase configuration with U_{so} hence Fr is displayed in Figure 8(a). A progressive change of flow regime from concentric CAF to eccentric CAF is predicted with a decrease in U_{so} from 0.8 m/s to 0.12 m/s, hence a decrease in Fr from 5.3 to 0.8. Figure 8(b) shows the change of phase configuration with Fr due to change of oil density. The oil core gets more concentric as the density difference between the fluids gets lower hence the Fr gets higher. Also, the oil core flows in the lower part of the annulus when the oil density is much higher than the water density.

4.3 Pressure gradient and water volume fraction

A comparison of predicted pressure gradients and water holdups against experimental results is shown in Table 2. Predictions of water holdups are consistent with measurements, having relative discrepancy within 14%. Irregularities are present in the predicted pressure gradients with relative errors ranging between 3% and 70%. The large discrepancies in pressure gradients calculated here very likely have their source in the poor estimation of oil fouling on the pipe wall. For cases S-5 and S-6a the pressure gradients were under predicted with little oil contact with the pipe wall observed in the calculated phase configurations, while thin oil fouling film was observed in experiments. Conversely, for the case S-2a both the pressure gradient and the oil contact with the pipe wall were over predicted compared to experimental results. As has been discussed in Section 3.1, the capture of the oil fouling on the pipe wall is affected by the wall contact angle modelling as well as the mesh resolution.

The water lubrication effect of water-lubricated high-viscosity oil-water flow in reducing the pressure gradient of single oil flow is demonstrated in Figure 9 illustrating the gauge pressure along the horizontal pipe for the simulation case S-6a. The slope of the line reflects the pressure gradient. Zone I represent the horizontal pipe section before the intersection; oil alone flows in that section before $z=0$ where it meets single-phase water flow coming through a T-shaped junction. The pressure gradient is constant along the pipe in zone I with $-\mathrm{d}p/dz = 23$ kPa/m. Zone II represents the developing region of the oil-water flow. The pressure gradient first has a sudden increase at the intersection since the bulk velocity increases and transient change occurs here; it decreases gradually along the pipe until reaching zone III where water-lubricated flow is developed. The pressure gradient in Zone III is significantly reduced with $-\mathrm{d}p/dz = 0.6$ kPa/m. The pressure drop reduction factor, $\mathrm{PDRF} = \frac{-(\mathrm{d}p/\mathrm{d}z)_{ow}}{-(\mathrm{d}p/\mathrm{d}z)_{so}}$, defined as the pressure gradient of oil-water flow to single phase oil flow at the same oil flow rate, is commonly used to demonstrate the water lubrication degree (Arney et al., 1903; Rodriguez et al., 2009). A comparison between PDRF obtained from CFD simulations and experiments is shown in Figure 10. A fair agreement is shown between measured and predicted PDRF. This shows that the CFD models can provide reasonable estimates of the water lubrication degree.

4.4 Cross-sectional flow characteristics of horizontal CAF

Among different flow regimes of water-lubricated flow, the CAF has been a focus of great interest driven by on one side its potential to save significant energy for high-viscosity oil transport, and on the other side the flow mechanists to understand this particular flow regime of liquid-liquid flow. In this section, the cross-sectional flow characteristics of horizontal CAF, which are seldom measured in experiments, are discussed based on the simulation results.

The cross-sectional phase distributions and dimensionless velocity profiles at different positions downstream of the junction are shown in Figure 11. Three typical cases, eccentric CAF (Case S-8a), virtually concentric CAF due to higher oil density (Case S-8a-Rho2), and virtually concentric CAF due to higher oil inertia (Case S-15), are depicted in Figures 11(a), (b) and (c), respectively. The volume fraction of the oil phase varies along the flow direction, reflecting the fluctuation of the phase interface along the flow direction. Due to the fluctuating interface, the dimensionless velocity profile along the

pipe varies even for established flow. The flow profiles get similar after around 120 times the pipe diameter downstream the junction for cases with $Re_{sw}=5190$ (Figure 11a and b) and around 170 times the pipe diameter for the case with $Re_{sw}=37\ 924$ (Figure 11c), indicating the flow is developed or approaching to be fully developed if not yet. Below we discuss the flow characteristics of CAF based on those flow profiles which can virtually represent those of a developed CAF. With reference of the phase distribution profiles, the velocity profiles illustrate that the velocity across the highly viscous oil core is virtually constant. That the oil core flows inside the water as a rigid body when the oil viscosity is much higher than the water viscosity has been used as an assumption in some analytical studies (Ooms et al,1984; Ooms et al., 2012). This assumption is validated by the CFD simulation results. It is worth emphasizing that the assumption of the rigid oil core in CAF is valid only when the oil viscosity is significantly higher than the annular water viscosity. Our separate numerical study of oil-water flow with matched density and medium viscosity ratio has shown that the oil core cannot be treated as a rigid body when the oil viscosity is just one order higher than the water viscosity (Shi et al., 2017b).

The velocity profile is virtually symmetric for concentric CAF as shown in Figure 11(bii) and (cii). The oil core flows as a solid body with a velocity higher than the average velocity of the annular water layer. Across the annular water layer, the velocity decreases quickly towards the pipe wall. For the eccentric CAF as shown in Figure 11(a), the top water layer is thinner than the bottom water layer. The velocity distribution for eccentric CAF is far off symmetric. Above the oil core, the velocity decreases quickly towards the pipe wall in the thin top water layer. Below the oil core, the velocity first increases then decreases towards the pipe wall. The oil-water slip ratios (i.e., the phase average velocity ratios, U_o/U_w) are higher than 1 for the concentric CAF shown in Figure 11(b) and (c), while slightly lower than 1 for the eccentric CAF shown in Figure 11(a). The average oil core velocity of developed CAF in Figure 11(a) and (b) is close to the mixture velocity, while it is as high as around 1.4 times of the mixture velocity in Figure 11(c). This is related to the absolute height of the water layer, hence the degree of the water lubrication effect. The cases in Figure 11(a) and (b) are CAF in Geometry I, while the case in Figure 11(c) is CAF in Geometry II. Though the relative water layer heights for the two concentric CAF

illustrated in Figure 11(b) and (c) are similar (around 10%-20% of the pipe diameter), the absolute height of the water layer is higher for the latter case.

The distribution of the oil volume fraction of CAF shown in Figure 11(c) is slightly different from that shown in Figure 11(a) and (b), having higher oil fractions in regions adjacent to the wall. This reflects the captured oil fouling film on the pipe wall. As has been discussed in Section 4.1, oil fouling film is more clearly captured with the simulation in a large-diameter pipe.

Figure 12 shows the turbulent kinetic energy and turbulent intensity of virtually developed core flow along the vertical line on the symmetry plane of two different cross-sections. Turbulent kinetic energy is the mean kinetic energy per unit mass associated with eddies in turbulent flow. The turbulent intensity is defined as the ratio of the root-mean-square of the velocity fluctuations to the mean flow velocity. The turbulent kinetic energy indicates the turbulence strength and the turbulent intensity indicates the relative turbulence strength. The distributions of the turbulent kinetic energy and turbulent intensity match the phase distributions shown in Figure 11, having higher values in the annular water layer, and very low values in the high-viscosity oil-core. For the eccentric CAF case in which the oil flows in the upper part of the pipe, the turbulent intensity is higher in the bottom water layer than in the upper thinner water layer (Figure 12a).

4.5 *Pressure at the core–annular interface*

One of the questions regarding CAF in a horizontal pipe is how the buoyancy force on the core, resulting from density difference between oil and water, is counterbalanced. Ooms et al. (2013) explained the levitation of the core by the net downward force on the core liquid resulted from pressure variations in the annular layer. Figure 13 displays the static pressure at the core–annular interface for an eccentric core flow case. It is shown that the pressure is higher where the core gets close to the pipe wall. This for the first time from a separate CFD study verifies the explanation by Ooms et al. (2013) on the stability of the eccentric core flows. The pressure distribution also shows variations in the directions of the net pressure along the flow direction, indicating the existence of the moment of the pressure on the core liquid.

5 Conclusions

A numerical study on horizontal oil-water flow with high viscosity ratio was conducted with the CFD code Fluent. The VOF multiphase model in conjunction with the SST k–ω scheme was applied for the simulations. The sensitivities of the numerical results to the flow domain initialization method, volume fraction interpolation schemes at phase interfaces, and wall contact angles are investigated. For water-lubricated flow, the water initialization method and the oil initialization method ultimately lead to similar results but the water initialization method requires less computational time. The Geo-Reconstruct scheme for the volume fraction interpolation gives more accurate prediction of the phase interface. The influence of the wall contact angle is not significant with regard to the phase configuration at the macro level for the oil-water flow with high-viscosity ratio (i.e., high capillary number flows). However, the predicted oil fouling film on the pipe wall is sensitive to the wall contact angle. It was not possible yet to adequately quantify the wall adhesion influence on the outputs.

The phase configurations calculated from the CFD models agree well with the experimental flow patterns. Moreover, the calculated flows are consistent with the anticipated flow patterns from mechanistic analysis based on the dimensionless numbers of G/V and Fronde number, demonstrating the capability of the aforementioned dimensionless numbers on describing the flow characteristics of two-phase flow. The quantitative agreement between predictions and experiments varied within 70% for the pressure gradient and 14% for the water volume fraction. The relatively high variation in the quantitative accuracy of the predicted pressure gradient is linked to the capture of the oil fouling film on the pipe wall.

The numerical results show that for CAF with high-viscosity ratio, the velocity across the oil core is virtually constant. The pressure at the core–annulus interface is higher where the core gets close to the pipe wall, resulting in a downward net pressure which can counter balance the buoyancy force on the core.

Appendix

The governing equations of the SST k-ω model are:

Turbulent kinetic energy:

$$\frac{\partial(\rho k)}{\partial t} + \nabla \cdot (\rho k \mathbf{u}) = \nabla \cdot \left(\left(\mu + \frac{\mu_t}{\sigma_k}\right)\nabla \cdot k\right) + G_k - Y_k \tag{A.1}$$

Specific dissipation rate:

$$\frac{\partial(\rho \omega)}{\partial t} + \nabla \cdot (\rho \omega \mathbf{u}) = \nabla \cdot \left(\left(\mu + \frac{\mu_t}{\sigma_\omega}\right)\nabla \cdot \omega\right) + G_\omega - Y_\omega + D_\omega \tag{A.2}$$

where G_k, G_ω represent the generation of k and ω, respectively; Y_k, Y_ω represent the dissipation of k and ω, respectively; D_ω represents the cross-diffusion term; μ_t represents the turbulent viscosity, $\mu_t = \frac{\rho k}{\omega}$. More information on the formulation for these quantities can be found in Wilcox (1988), Menter (1994) or Fluent theory guide (2012).

The turbulence damping option was activated in this study. An additional source term is added to the ω-equation for reduction of the destruction term (Y_ω). This additional source term is expressed as

$$S_\omega = A_i \Delta n \beta \rho_i \omega_\omega^2 \tag{A.3}$$

$$\omega_\omega = B \frac{6\mu_i}{\beta \rho_i \Delta n^2} \tag{A.4}$$

$$A_i = 2\alpha_i |\nabla \alpha_i| \tag{A.5}$$

where A_i represents an interface area density that activates the correction term in the vicinity of the interface only ($A_i = 0$ outside the interface region); α_i is the volume fraction of phase i; Δn is the grid size in the interface region; β is a closure coefficient, $\beta = 0.075$; B is a damping factor which can be specified, the default value was used.

Nomenclature

A_i interface area density, m^{-1}

B turbulence damping factor

d internal pipe diameter, m

D_ω cross-disfussion term in the specific dissipation rate equation, kg m^{-2}s^{-2}

F   external body force per unit volume, kg m^{-2}s^{-2}

g gravitational acceleration, m s^{-2}

G_k production of turbulent kinetic energy, kg m^{-1}s^{-3}

G_ω generation term of the turbulence specific dissipation rate, kg m^{-2}s^{-2}

I   turbulence intensity

k kinetic energy of turbulence, m^2 s^{-2}

$\hat{n}$ unit surface normal vector, m^{-1}

$\hat{n}_{wl}$ unit vector normal to the wall, m^{-1}

p pressure, N m^{-2}

S_ω source term for reduction of the destruction term in the specific dissipation rate equation, kg m^{-2}s^{-2}

t time, s

$\hat{t}_{wl}$ unit vector tangential to the wall, m^{-1}

u velocity, m s^{-1}

U average velocity, m s^{-1}

U_m mixture average velocity, m s^{-1}

U_{max} mixture maximum velocity, m s^{-1}

U_o average velocity of the oil phase, m s^{-1}

U_w average velocity of the water phase, m s^{-1}

U_{so} superficial oil velocity, m s^{-1}

U_{sw} superficial water velocity, m s^{-1}

Y_k dissipation of turbulent kinetic energy, kg m^{-1}s^{-3}

Y_ω dissipation term for the turbulence specific dissipation rate, kg m^{-2}s^{-2}

z   longitudinal position from the junction, m

Greek letters

α volume fraction

β closure coefficient in turbulence damping term, 0.075

θ_{wl} angle between the wall and the tangent to the interface at the wall, °

κ interface curvature, m^{-1}

μ molecular viscosity, kg m^{-1}s^{-1}

μ_t turbulent viscosity, kg m^{-1}s^{-1}

ρ density, kg m^{-3}

σ surface tension coefficient, N m^{-1}

σ_k Prandtl number for kinetic energy equation

σ_ω Prandtl number for specific dissipation rate equation

ω specific dissipation rate, s^{-1}

ω_ω additional specific dissipation rate term in the interface turbulence damping

     model, s^{-1}

Δn grid size in the interface region, m

Dimensionless groups

Ca   capillary number, $Ca = \frac{\mu U}{\sigma}$

Fr   Froude number, $Fr = \sqrt{\frac{U_{so}^2}{gD\frac{\Delta\rho}{\rho_w}}}$

G/V gravitation to viscous force ratio, $G/V = \frac{\Delta\rho gD^2}{\mu U}$

Re   Reynolds number, $Re = \frac{\rho U d}{\mu}$

Subscripts

k kinetic energy equation

o oil

so	superfacial oil
sw	superfacial water
t	turbulence
w	water
wl	wall
ω	specific dissipation rate equation

References

ANSYS® Fluent, r. Fluent Theory Guide (2012). USA: ANSYS Inc.

Arney, M.S., Bai, R., Guevara, E., Joseph, D., Liu, K., 1993. Friction factor and holdup studies for lubricated pipelining—I. Experiments and correlations. Int. J. Multiph. Flow. 19(6), 1061-1076.

Bai, R., Kelkar, K., Joseph, D.D., 1996. Direct simulation of interfacial waves in a high-viscosity-ratio and axisymmetric core–annular flow. J. Fluid Mech. 327, 1-34.

Bannwart, A.C., 1998. Wavespeed and volumetric fraction in core annular flow. Int. J. Multiph. Flow. 24(6), 961-974.

Bannwart, A.C., Rodriguez, O.M., de Carvalho, C.H., Wang, I.S., Vara, R.M., 2004. Flow patterns in heavy crude oil-water flow. J. Energy Resour. Technol. 126(3), 184-189.

Brackbill, J., Kothe, D.B., Zemach, C., 1992. A continuum method for modeling surface tension. J. Comput. Phys. 100(2), 335-354.

Cavicchio, C.A., Biazussi, J.L., de Castro, M.S., Bannwart, A.C., Rodriguez, O.M., de Carvalho, C.H., 2018. Experimental study of viscosity effects on heavy crude oil-water core-annular flow pattern. Exp. Therm Fluid Sci. 92, 270-285.

Dehkordi, P.B., Colombo, L.P.M., Guilizzoni, M., Sotgia, G., 2017. CFD simulation with experimental validation of oil-water core-annular flows through Venturi and Nozzle flow meters. J. Pet. Sci. Eng. 149, 540-552.

Ghosh, S., Das, G., Das, P.K., 2010. Simulation of core annular downflow through CFD—A comprehensive study. Chem. Eng. Process.: Process Intensif. 49(11), 1222-1228.

Ghosh, S., Das, G., Das, P.K., 2011. Simulation of core annular in return bends—A comprehensive CFD study. Chem. Eng. Res. Des. 89(11), 2244-2253.

Grassi, B., Strazza, D., Poesio, P., 2008. Experimental validation of theoretical models in two-phase high-viscosity ratio liquid–liquid flows in horizontal and slightly inclined pipes. Int. J. Multiph. Flow. 34(10), 950-965.

Housz, E.I., Ooms, G., Henkes, R., Pourquie, M., Kidess, A., Radhakrishnan, R., 2017. A comparison between numerical predictions and experimental results for horizontal core-annular flow with a turbulent annulus. Int. J. Multiph. Flow. 95, 271-282.

Jiang, F., Wang, Y., Ou, J., Chen, C., 2014. Numerical Simulation of Oil-Water Core Annular Flow in a U-Bend Based on the Eulerian Model. Chem. Eng. Technol. 37(4), 659-666.

Jiang, F., Wang, K., Skote, M., Wong, T.N., Duan, F., 2018. Simulation of non-Newtonian oil-water core annular flow through return bends. Heat Mass Transfer. 54(1), 37-48.

Jiang, T.-S., Soo-Gun, O., Slattery, J.C., 1979. Correlation for dynamic contact angle. J. Colloid Interface Sci. 69(1), 74-77.

Joseph, D.D., Bai, R., Mata, C., Sury, K., Grant, C., 1999. Self-lubricated transport of bitumen froth. J. Fluid Mech. 386, 127-148.

Kaushik, V., Ghosh, S., Das, G., Das, P.K., 2012. CFD simulation of core annular flow through sudden contraction and expansion. J. Pet. Sci. Eng. 86, 153-164.

Ko, T., Choi, H., Bai, R., Joseph, D., 2002. Finite element method simulation of turbulent wavy core–annular flows using a k-ω turbulence model method. Int. J. Multiph. Flow. 28(7), 1205-1222.

Lee, B., Kang, M., 2016. Full 3d simulations of two-phase core–annular flow in horizontal pipe using level set method. J. Sci. Comput. 66(3), 1025-1051.

Li, J., Renardy, Y., 2000. Numerical study of flows of two immiscible liquids at low Reynolds number. SIAM Rev. 42(3), 417-439.

McKibben, M.J., Gillies, R.G., Shook, C.A., 2000a. A laboratory investigation of horizontal well heavy oil—water flows. Can. J. Chem. Eng. 78(4), 743-751.

McKibben, M.J., Gillies, R.G., Shook, C.A., 2000b. Predicting pressure gradients in heavy oil—water pipelines. Can. J. Chem. Eng. 78(4), 752-756.

Menter, F.R., 1994. Two-equation eddy-viscosity turbulence models for engineering applications. AIAA J. 32(8), 1598-1605.

Oliemans, R., Ooms, G., Wu, H., Duijvestijn, A., 1987. Core-annular oil/water flow: the turbulent-lubricating-film model and measurements in a 5 cm pipe loop. Int. J. Multiph. Flow. 13(1), 23-31.

Ooms, G., Pourquie, M., Beerens, J., 2013. On the levitation force in horizontal core-annular flow with a large viscosity ratio and small density ratio. Phys. Fluids. 25(3), 032102.

Ooms, G., Pourquie, M., Poesio, P., 2012. Numerical study of eccentric core-annular flow. Int. J. Multiph. Flow. 42, 74-79.

Ooms, G., Segal, A., Van Der Wees, A., Meerhoff, R., Oliemans, R., 1984. A theoretical model for core-annular flow of a very viscous oil core and a water annulus through a horizontal pipe. Int. J. Multiph. Flow. 10(1), 41-60.

Rodriguez, O., Bannwart, A.C., de Carvalho, C., 2009. Pressure loss in core-annular flow: modeling, experimental investigation and full-scale experiments. J. Pet. Sci. Eng. 65(1), 67-75.

Shi, J., Al-Awadi, H., Yeung, H., 2017a. An experimental investigation of high-viscosity oil-water flow in a horizontal pipe. Can. J. Chem. Eng. 95(12), 2423-2434.

Shi, J., Gourma, M., Yeung, H., 2017b. CFD simulation of horizontal oil-water flow with matched density and medium viscosity ratio in different flow regimes. J. Pet. Sci. Eng. 151, 373-383.

Shi, J., Lao, L., Yeung, H., 2017c. Water-lubricated transport of high-viscosity oil in horizontal pipes: the water holdup and pressure gradient. Int. J. Multiph. Flow. 96, 70-85.

Shi, J., Yeung, H., 2017. Characterization of liquid-liquid flows in horizontal pipes. AlChE J. 63(3), 1132-1143.

Sotgia, G., Tartarini, P., Stalio, E., 2008. Experimental analysis of flow regimes and pressure drop reduction in oil-water mixtures. Int. J. Multiph. Flow. 34(12), 1161-1174.

Sridhar, S., Zhang, H.-q., Sarica, C., Pereyra, E.J., 2011. Experiments and Model Assessment on High-Viscosity Oil/Water Inclined Pipe Flows. SPE Annual Technical Conference and Exhibition, Colorado, USA, 30 October-2 November, 2011.

Strazza, D., Grassi, B., Demori, M., Ferrari, V., Poesio, P., 2011. Core-annular flow in horizontal and slightly inclined pipes: Existence, pressure drops, and hold-up. Chem. Eng. Sci. 66(12), 2853-2863.

Van Mourik, S., Veldman, A., Dreyer, M., 2005. Simulation of capillary flow with a dynamic contact angle. Microgravity-Science and Technology. 17(3), 87-93.

Wang, W., Gong, J., Angeli, P., 2011. Investigation on heavy crude-water two phase flow and related flow characteristics. Int. J. Multiph. Flow. (9), 1156-1164.

Wilcox, D.C., 1998. Turbulence modeling for CFD. California: DCW industries

Table Captions

Table 1. Programme of simulations.

Table 2. Comparison of experimental and CFD predicted pressure gradients and water holdups.

Figure Captions

Figure 1. Schematic diagram of the simulation geometry.

Figure 2. Predicted flow patterns from simulations using different wall contact angles (the red and blue represent oil and water respectively) and the corresponding experimental flow pattern (oil core inside annular water). (a) 175°; (b) 120°; (c) 60°; (d) 5°; (e) snapshot of experimental flow.

Figure 3. Development of phase configuration with simulation time. (a) Water initialization (Run S-6a); (b) Oil initialization (Run S-6b).

Figure 4. Predicted flow patterns from simulations using different volume fraction interpolation schemes at the interface and the corresponding experimental flow pattern. (a) Geo-Reconstruct scheme (Run S-2a); (b) CICSAM scheme (Run S-2b); (c) Snapshot of experimental flow.

Figure 5. Comparison of experimental and CFD predicted flow patterns. Illustrations of experimental flow patterns are snapshots of developed experimental flow; the darker color represents oil and the lighter color represents water. Illustrations of CFD flow patterns show oil and water phases in red and blue respectively.

Figure 6. Calculated phase configurations across a specific cross-section of the horizontal pipe with simulation time (the red and blue represent oil and water respectively). (a) Run S-6a; (b) Run S-8a; (c) Run S-15.

Figure 7. Change of phase configuration with change of the gravitation to viscous force ratio (G/V = $\frac{\Delta \rho g D^2}{\mu_o U_m}$). (a) different oil viscosities (i, 5000 cP, G/V=0.2; ii, 1000 cP, G/V=1; iii, 500 cP, G/V=2; iv, 100 cP, G/V=9.7) and (b) different pipe diameters (i, d=26 mm, G/V=0.2; ii , d=76 mm, G/V=1.7) under controlled phase velocities U_{so}=0.4 m/s, and U_{sw}=0.2 m/s. (b-iii) d=76 mm, U_{so}=2.0 m/s, and U_{sw}=0.5 m/s, G/V=0.4.

Figure 8. Change of phase configuration with change of Froude number (Fr). (a) different oil velocities at U_{sw}=0.2 m/s (i, U_{so}=0.12 m/s, Fr=0.8; ii, U_{so}=0.4 m/s, Fr=2.7; iii, U_{so}=0.8 m/s, Fr=5.3). (b) different oil densities at U_{so}=0.4 m/s and U_{sw}=0.2 m/s (i, 910kg/m³, Fr=2.7; ii, 960kg/m³, Fr=4.1; iii, 1100kg/m³, Fr=2.5).

Figure 9. Predicted pressure along the horizontal pipe (Run S-5).

Figure 10. Pressure drop reduction factor (PDRF) from simulations and measurements versus input water volume faction (C_w) at different superficial oil velocities. (a) U_{so}=0.1 m/s; (b) U_{so}=0.4 m/s.

Figure 11. Phase distribution (i) and velocity profiles (ii) of high-viscosity oil CAF at different distances downstream of the junction. (a) Case S-8a, Geometry I, Re_{sw}=5190, ρ_o=910 kg/m^3; (b) Case S-8a-Rho2, Geometry I, Re_{sw}=5190, ρ_o=960 kg/m^3 ; (c) Case S-15, Geometry II, Re_{sw}=37 924, ρ_o=910 kg/m^3.

Figure 12. Turbulent kinetic energy (i) and intensity (ii) of virtually developed CAF. (a) Case S-8a, Geometry I, Re_{sw}=5190, ρ_o=910 kg/m^3; (b) Case S-8a-Rho2, Geometry I, Re_{sw}=5190, ρ_o=960 kg/m^3 ; (c) Case S-15, Geometry II, Re_{sw}=37 924, ρ_o=910 kg/m^3.

Figure 13. Static pressure at the core–annular interface. The black lines illustrate the outline of the internal pipe wall. Run S-8a, Re_{sw}=5190.

Table 1. Programme of simulations.

Notation of Simulation [a]	Flow conditions and fluid properties [b]						Experimental flow pattern [c]
	U_{so} (m/s)	U_{sw} (m/s)	μ_o (cP)	ρ_o (kg/m^3)	Re_{so}	Re_{sw}	
S-1	0.06	0.23	5000	910	0.3	5968	OPL
S-2a; S-2b (Change volume fraction interpolation schemes)	0.11	0.10	5000	910	0.5	2595	CAF
S-3	0.12	0.18	5000	910	0.6	4671	CAF
S-4	0.12	0.41	5000	910	0.6	10639	CAF
S-5	0.12	0.61	5000	910	0.6	15 828	OLP
S-6a; S-6b (Change initialization methods)	0.12	0.81	5000	910	0.6	21 018	OLP
S-7	0.40	0.02	5000	910	1.9	519	-
S-8a; S-8b; S-8c; S-8d (Change wall contact angles)	0.40	0.20	5000	910	1.9	5190	CAF
S-8a-Rho2	0.40	0.20	5000	960	2.0	5190	-
S-8a-Rho3	0.40	0.20	5000	1100	2.3	5190	-
S-8a-Mu2	0.40	0.20	1000	910	9.5	5190	-
S-8a-Mu3	0.40	0.20	500	910	18.9	5190	-
S-8a-Mu4	0.40	0.20	100	910	94.6	5190	-
S-9	0.40	0.40	5000	910	1.9	10 379	CAF
S-10	0.40	0.60	5000	910	1.9	15 569	CAF
S-11	0.40	0.80	5000	910	1.9	20 758	CAF
S-12	0.80	0.04	5000	910	3.8	1038	-
S-13	0.80	0.20	5000	910	3.8	5190	-
S-14 (Geometry II)	0.40	0.20	5000	910	1.9	5190	-
S-15 (Geometry II)	2.00	0.50	5000	910	9.5	37 924	-

[a] Geometry I is used for the simulations when it is not noted.

[b] Other properties not included in the table: ρ_w= 998 kg/m^3, μ_w=1 cP and σ=0.02 N/m.

[c] OPL, oil plugs in water; CAF, core annular flow; OLP, dispersed oil lumps in water. For more detailed description, please refer to Shi et al. (2017c).

Table 2. Comparison of experimental and CFD predicted pressure gradients and water holdups.

Notation of Simulation [a]	Flow pattern [b] (Exp. / CFD)	Pressure gradient (kPa/m)			Water holdup		
		Exp.	CFD	Error	Exp.	CFD	Error
S-1	OPL / OPL	0.964	0.845	-12 %	-	-	-
S-2a	CAF / CAF	1.24	2.06	66 %	0.39	0.36	-9 %
S-3	CAF / CAF	1.31	2.15	64 %	0.50	0.43	-14%
S-4	CAF / CAF	1.75	1.08	-38 %	0.67	0.76	13%
S-5	OLP / OLP	1.97	0.61	-69 %	0.77	0.81	6%
S-6a	OLP / OLP	2.33	0.86	-63 %	0.77	0.86	12%
S-7	- / OC	-	62.73	-	-	-	-
S-8a	CAF / CAF	3.11	3.26	5 %	0.34	0.33	-2%
S-9	CAF / CAF	2.68	2.54	-5 %	0.51	0.47	-8%
S-10	CAF / CAF	2.6	2.67	3 %	0.59	0.58	-2%
S-11	CAF / CAF-OLP	2.94	4.6	56 %	0.63	0.61	-2%
S-12	- / OC	-	130.36	-	-	-	-
S-13	- / CAF	-	12.06	-	-	-	-
S-14 (Geometry II)	- / ST	-	5.58	-	-	-	-
S-15 (Geometry II)	- / CAF	-	8.2	-	-	-	-

[a] Geometry I is used when not specified.

[b] Flow pattern: OPL, oil plugs in water; CAF, core annular flow; OLP, dispersed oil lumps in water; CAF-OLP, transitional flow between CAF and OLP; OC, oil-continuous flow.

[c] Error: $(\varphi_{cfd}-\varphi_{exp}) / \varphi_{expv}$

Figure 1. Schematic diagram of the simulation geometry.

Figure 2. Predicted flow patterns from simulations using different wall contact angles (the red and blue represent oil and water respectively) and the corresponding experimental flow pattern (oil core inside annular water). (a) 175°; (b) 120°; (c) 60°; (d) 5°; (e) snapshot of experimental flow.
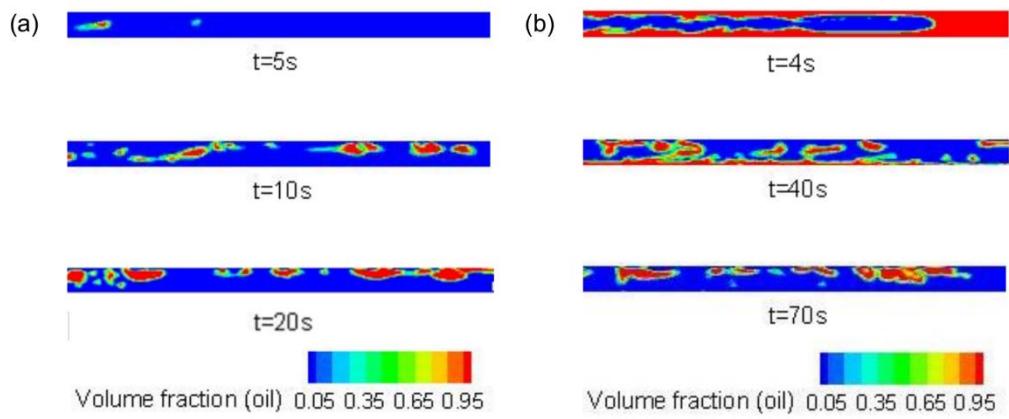
Figure 3. Development of phase configuration with simulation time. (a) Water initialization (Run S-6a); (b) Oil initialization (Run S-6b).

Figure 4. Predicted flow patterns from simulations using different volume fraction interpolation schemes at the interface and the corresponding experimental flow pattern. (a) Geo-Reconstruct scheme (Run S-2a); (b) CICSAM scheme (Run S-2b); (c) Snapshot of experimental flow.

Figure 5. Comparison of experimental and CFD predicted flow patterns. Illustrations of experimental flow patterns are snapshots of developed experimental flow; the darker color represents oil and the lighter color represents water. Illustrations of CFD flow patterns show oil and water phases in red and blue respectively.

(a)

t=36.149 s   t=36.229 s   t=36.309 s

(b)

t=39.693 s   t=40.173 s   t=40.653 s

(c)

t=16.968 s   t=17.008 s   t=17.048 s

Figure 6. Calculated phase configurations across a specific cross-section of the horizontal pipe with simulation time (the red and blue represent oil and water respectively). (a) Run S-6a; (b) Run S-8a; (c) Run S-15.

Figure 7. Change of phase configuration with change of the gravitation to viscous force ratio (G/V = $\frac{\Delta\rho g D^2}{\mu_o U_m}$). (a) different oil viscosities (i, 5000 cP, G/V=0.2; ii, 1000 cP, G/V=1; iii, 500 cP, G/V=2; iv, 100 cP, G/V=9.7) and (b) different pipe diameters (i, d=26 mm, G/V=0.2; ii , d=76 mm, G/V=1.7) under controlled phase velocities U_{so}=0.4 m/s, and U_{sw}=0.2 m/s. (b-iii) d=76 mm, U_{so}=2.0 m/s, and U_{sw}=0.5 m/s, G/V=0.4.

Figure 8. Change of phase configuration with change of Froude number (Fr). (a) different oil velocities at U_{sw}=0.2 m/s (i, U_{so}=0.12 m/s, Fr=0.8; ii, U_{so}=0.4 m/s, Fr=2.7; iii, U_{so}=0.8 m/s, Fr=5.3). (b) different oil densities at U_{so}=0.4 m/s and U_{sw}=0.2 m/s (i, 910kg/m^3, Fr=2.7; ii, 960kg/m^3, Fr=4.1; iii, 1100kg/m^3, Fr=2.5).
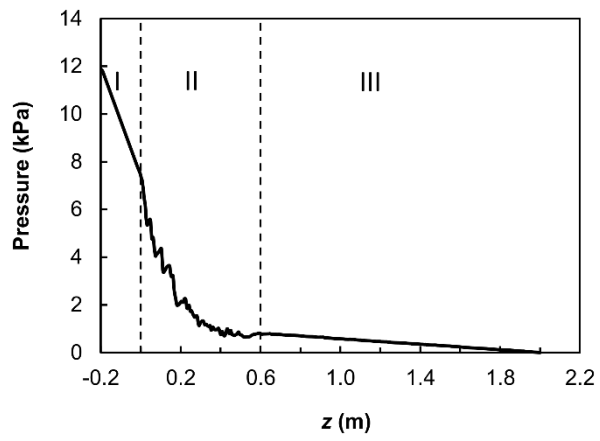
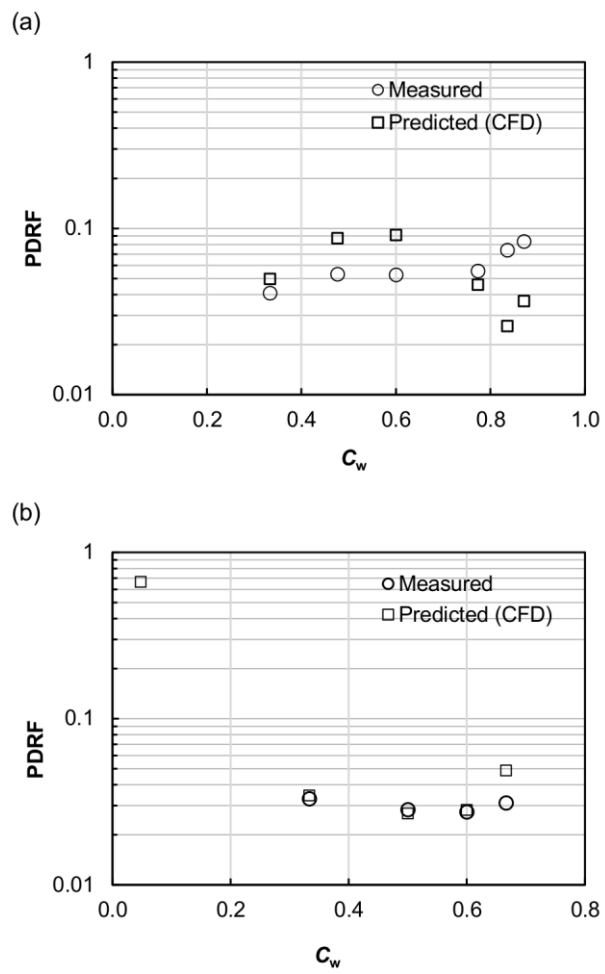**Figure 9.** Predicted pressure along the horizontal pipe (Run S-5).

(a)

(b)

Figure 10. Pressure drop reduction factor (PDRF) from simulations and measurements versus input water volume faction (C_w) at different superficial oil velocities. (a) U_{so}=0.1 m/s; (b) U_{so}=0.4 m/s.
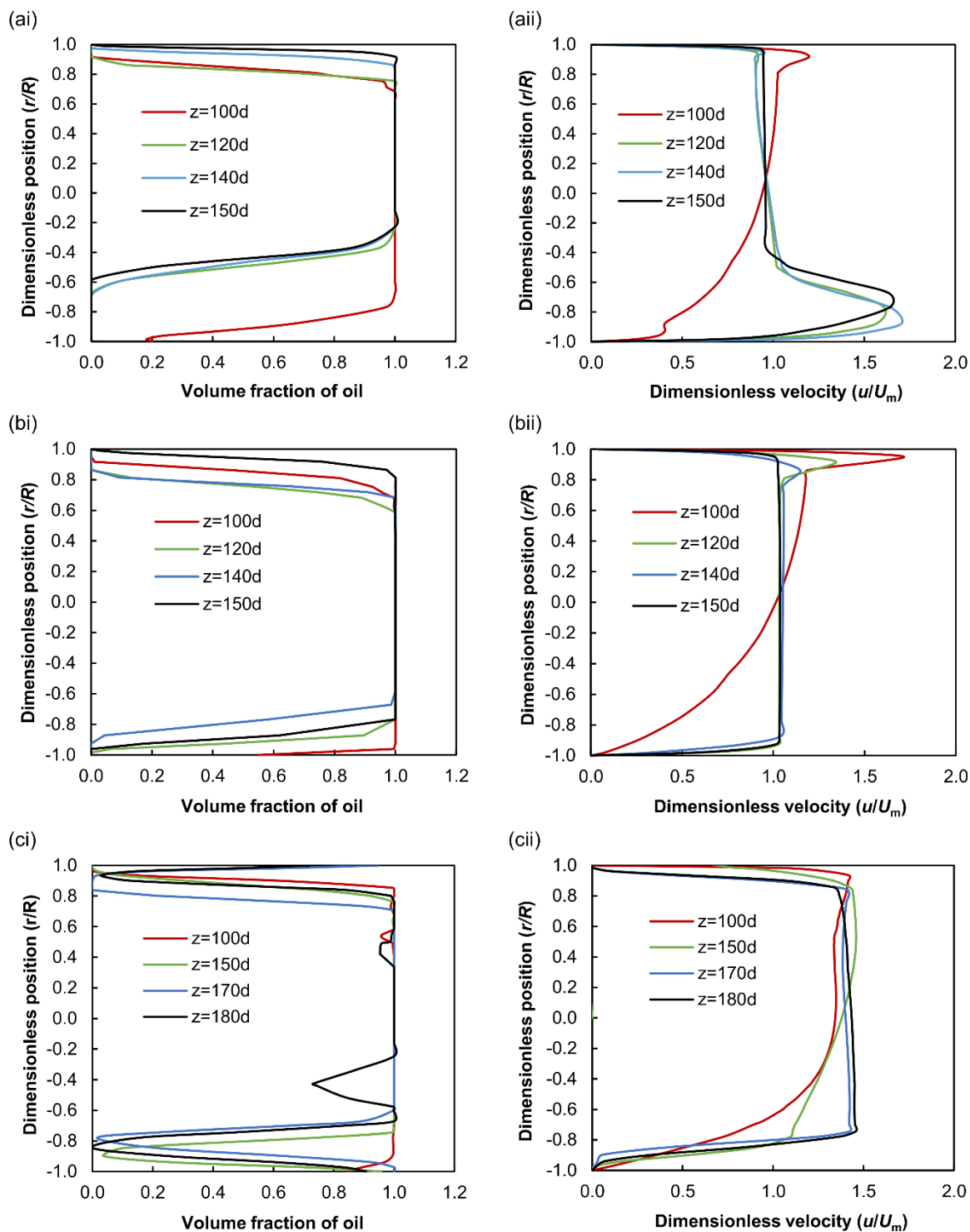
Figure 11. Phase distribution (i) and velocity profiles (ii) of high-viscosity oil CAF at different distances downstream of the junction. (a) Case S-8a, Geometry I, Re_{sw}=5190, ρ_o=910 kg/m^3; (b) Case S-8a-Rho2, Geometry I, Re_{sw}=5190, ρ_o=960 kg/m^3; (c) Case S-15, Geometry II, Re_{sw}=37 924, ρ_o=910 kg/m^3.
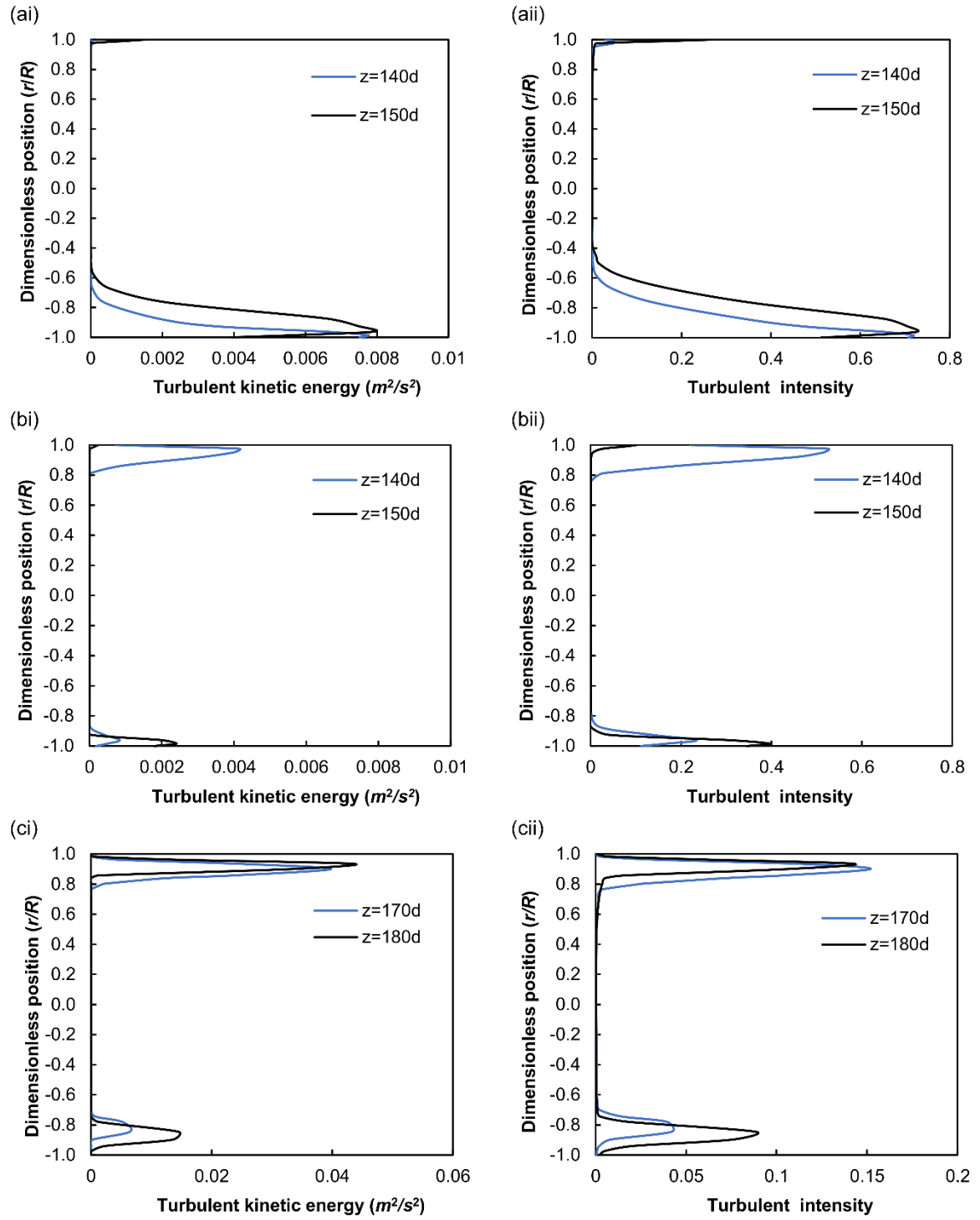
Figure 12. Turbulent kinetic energy (i) and intensity (ii) of virtually developed CAF. (a) Case S-8a, Geometry I, Re_{sw}=5190, ρ_o=910 kg/m^3; (b) Case S-8a-Rho2, Geometry I, Re_{sw}=5190, ρ_o=960 kg/m^3; (c) Case S-15, Geometry II, Re_{sw}=37 924, ρ_o=910 kg/m^3.
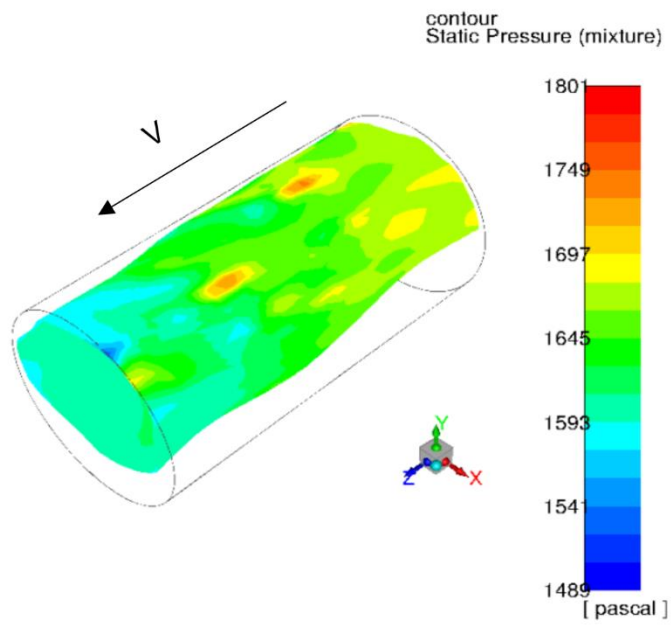
Figure 13. Static pressure at the core–annular interface. The black lines illustrate the outline of the internal pipe wall. Run S-8a, Re_{sw}=5190.